Journal of Materiomics 12 (2026) 101212

Contents lists available at ScienceDirect

Journal of Materiomics

journal homepage: www.journals.elsevier.com/journal-of-materiomics/

Role of the orthorhombic phase in endurance degradation of $Hf_{0.5}Zr_{0.5}O_2$ memristors

Jun-Cheol Park [a,1], WooJun Seol [a,1], Sihyeon Baek [b,1], Donghyeon Lee [a], Seong Min Park [a], Seon Je Kim [c], Young-Min Kim [c], Hu Young Jeong [b,*], Ji Young Jo [a,**], Sanghan Lee [a,d,***]

[a] Department of Materials Science and Engineering, Gwangju Institute of Science and Technology, 123 Cheomdangwagi-ro, Buk-gu, Gwangju, 61005, Republic of Korea
[b] Graduate School of Semiconductor Materials and Device Engineering, Ulsan National Institute of Science and Technology, 50 UNIST-gil, Eonyang-eup, Ulju-gun, Ulsan, 44919, Republic of Korea
[c] Department of Energy Science, Sungkyunkwan University, 2066 Seobu-ro, Jangan-gu, Suwon, 16419, Republic of Korea
[d] Research Institute for Solar and Sustainable Energies (RISE), Gwangju Institute of Science and Technology, 123 Cheomdan-gwagiro, Buk-gu, Gwangju, 61005, Republic of Korea

ARTICLE INFO

Article history:
Received 28 January 2026
Received in revised form
25 February 2026
Accepted 2 March 2026
Available online 19 March 2026

Keywords:
HZO
Memristor
Orthorhombic phase
Degradation

ABSTRACT

The development of next-generation memory architectures is essential to overcoming limitations of conventional architectures, notably the von Neumann bottleneck. Among emerging technologies, memristors have attracted considerable attention due to their scalability, low power consumption, and neuromorphic potential. However, limited endurance and retention, as well as process-integration constraints, continue to impede practical deployment. HfO_2-based memristors are promising due to silicon compatibility and thermal stability, yet switching stability remains a key challenge. Here, we systematically investigate the structural role of the orthorhombic phase in $Hf_{0.5}Zr_{0.5}O_2$ (HZO)-based memristors during the degradation process. Using *in situ* synchrotron X-ray diffraction (XRD) under an applied electric field, we tracked the field-driven structural evolution over repeated SET/RESET cycles. The orthorhombic phase diffraction intensity progressively decreases and peak broadening increases with cycling, while no distinct shift indicative of a macroscopic phase transition is observed within the experimental resolution. This degradation of crystallinity correlates with the rupture of conductive filaments and eventual device breakdown. These findings highlight the critical role of the orthorhombic phase in both switching behavior and device failure, providing insight into phase-engineered stability in memristive devices.

1. Introduction

The need for next-generation memory devices is further emphasized by the limitation of conventional architectures arising from the von Neumann bottleneck issue [1,2]. Memristor based in-memory computing has therefore garnered substantial attention because it enables computation within the memory array, reducing data transfer between processor and memory [3,4]. Furthermore, memristors possess favorable characteristics including miniaturization, low power consumption, high-speed read/write capability, and compatibility with neuromorphic architectures [5–7]. Despite extensive materials exploration from metal oxides to organic systems, commercialization remains constrained by limited on/off ratio, endurance, retention, and incomplete CMOS compatibility [8–11]. Among candidate materials, HfO_2 based memristors, which are compatible with silicon and thermally stable, are promising candidates to address these limitations. Nevertheless, switching instability and retention remain unresolved.

In memory devices such as Fe-RAM, DRAM, and various capacitors, understanding the breakdown pathways is one of the

* Corresponding author.
** Corresponding author.
*** Corresponding author. Department of Materials Science and Engineering, Gwangju Institute of Science and Technology, 123 Cheomdangwagi-ro, Buk-gu, Gwangju, 61005, Republic of Korea.
E-mail addresses: hulex@unist.ac.kr (H.Y. Jeong), jyjo@gist.ac.kr (J.Y. Jo), sanghan@gist.ac.kr (S. Lee).
[1] Jun-Cheol Park, WooJun Seol and Sihyeon Baek have contributed equally to this work.

https://doi.org/10.1016/j.jmat.2026.101212

most important factors for improving their reliability and stability [11–13]. Likewise, understanding and addressing the breakdown mechanism is crucial for resistive switching devices, where breakdown is closely linked to defect redistribution and conductive filament (CF) evolution. Recent studies have highlighted a connection between phase constitution and resistive switching in HZO. Zhu *et al.* reported that the orthorhombic phase with a uniform microstructure significantly affects the resistive switching behavior in HZO film [14]. In addition, Yoong *et al.* emphasized the role of orthorhombic phase in memristors, and similarly Zeng *et al.* carefully noted that amorphous or polycrystalline oxide based synaptic devices may hinder uniform CF formation, resulting in nonlinear switching behavior [15,16]. These findings motivate direct observation of how orthorhombic-phase stability evolves under electrical stress and how such evolution relates to degradation and failure.

Up to now, metal oxide-based memristors including HfO_2 have typically been described by the formation and rupture of CF mediated by oxygen vacancies. Yang *et al*. observed the CF forming process by scanning transmission electron microscopy (STEM) [17]. The formation of CF was driven by the migration of oxygen ions, and exhibited self-limiting behavior. Zhu *et al*. reported the importance of orthorhombic phase in $Hf_{0.5}Zr_{0.5}O_2$ (HZO) for improving synaptic properties [14]. In many HZO stacks, a higher o-phase contribution is achieved under condiction where the oxygen vacancy distribution is concurrently modified. Therefore, improved switching can be accompanied by increased leakage through oxygen vacancy related defect/trap states and defect assisted conduction pathways, rather than being intrinsic consequence of the o-phase [18,19]. Similarly, Lee *et al.* induced oxygen vacancies in HZO films by introducing WSe_2 layers, which led to improvements in both resistive switching behavior and retention [20]. These findings suggest that oxygen vacancy dynamics and phase stability are strongly coupled and may jointly govern switching reliability. Notably, recent interface-engineering studies further indicate that reducing oxygen vacancies can suppress leakage while maintaining or improving structural quality, highlighting that leakage is primarily governed by defect chemistry and interfaces [21].

In this work, the entire process of resistive switching behavior, including initial, degradation and breakdown process was investigated through *in situ* synchrotron X-ray diffraction (XRD) under applied electric field and *ex situ* scanning transmission electron microscopy (STEM) combined with 4D nanobeam electron diffraction (NBED) technique. HZO films with a $La_{0.67}Sr_{0.33}MnO_3$ (LSMO) bottom electrode were prepared by pulsed laser deposition. The coexistence of orthorhombic and monoclinic phases in HZO films was also characterized by high-resolution X-ray diffraction (HR-XRD) and transmission electron microscopy (TEM). According to *in situ* XRD and *ex situ* TEM analyses, electric-field-induced SET/RESET operations degraded the crystallinity of the orthorhombic phase. Finally, the orthorhombic phase was identified as a crucial factor not only in the formation of CF but also in the breakdown process. This work provides new insights into the relationship between the orthorhombic phase and breakdown phenomena in memristive HZO thin films.

2. Experimental section

2.1. Device fabrication of $Pt/Hf_{0.5}Zr_{0.5}O_2/La_{0.67}Sr_{0.33}MnO_3$ structure

The $Hf_{0.5}Zr_{0.5}O_2$ (HZO) and $La_{0.67}Sr_{0.33}MnO_3$ (LSMO) thin films were deposited on the $SrTiO_3$ (STO) substrate by PLD with a 248 nm KrF excimer laser (Coherent, Compex Pro 205F). Acetone, methanol, isopropyl alcohol, and deionized water were used to remove organic particles and/or residues on the substrates. The LSMO as a bottom electrode layer was deposited at a 5 Hz repetition rate, a laser energy density of 2.0 J•cm^{-2}, a substrate temperature of 620 °C, and a 200 mTorr O_2 gas environment. Subsequently, HZO was deposited at a 2 Hz repetition rate, a laser energy density of 2.0 J•cm^{-2}, a substrate temperature of 800 °C, and a 75 mTorr O_2 gas condition. Finally, HZO/LSMO/STO structure was cooled down at 5 °C•min^{-1}. For fabrication of metal/insulator/metal structure for memristor, Pt dot (50 nm thick) as a top electrode was deposited by e-beam evaporator using shadow mask at room temperature with a rate of 0.2 Å/s.

2.2. Materials characterization

XRD measurement was performed using 3A beamline (λ = 1.11296 Å) at Pohang Accelerator Laboratory (PAL), equipped with a four-circle goniometer. Reciprocal space map (RSM) was measured using X-ray beam focused to a size of 16 μm × 4 μm by a Kirkpatrick-Baez (KB) mirror at the 9C beamline (λ = 1.2398 Å) at the PAL.

For TEM analysis, cross-sectional lamella samples were prepared using a Ga + focused ion beam (FEI Helios NanoLab 450F1) with final low-kV cleaning to minimize surface damage.

TEM, STEM, and EDS analyses were performed using a double aberration-corrected TEM (Titan^3 G2 60-300, FEI) at 200 kV. EELS and 4D-STEM nanobeam electron diffraction (NBED) measurements were conducted on a double aberration-corrected STEM (JEM-GrandARM300F, JEOL) operated at 300 kV. NBED datasets were acquired using a Gatan OneView camera in combination with a STEM synchronization system.

2.3. Resistive switching performance

I–V measurements were carried out using a probe station with Keithley 4200A-SCS parameter analyzer (Tektronix Inc., Beaverton, USA) for DC bias sweep. Top Pt electrodes and $La_{0.67}Sr_{0.33}MnO_3$ bottom electrodes were used to apply voltage bias and grounded, respectively.

2.4. In situ X-ray diffraction

A Pilatus 100k gate array detector (Dectris Ltd.) collected the diffracted X-rays from the sample. A delay generator (DG645, Stanford Research Systems) was used to synchronize the electric pulses and X-ray detection. The X-ray beam was focused onto the Pt electrode where the electric field was applied. Pulse sequences consisting of consecutive square-shaped pulses with fixed pulse widths and amplitudes of were applied to the sample to investigate the read and write states. (Details of the pulse trains used in each experiment are provided in the Supporting Information, Fig. S5b, Figs. S8–S9) [22].

2.5. Computational method

The 4D-STEM dataset was preprocessed using logarithmic scaling to enhance diffraction signal contrast. Clustering was performed using in-house MATLAB (2024a) code based on Non-negative Matrix Factorization (NMF) and k-means algorithms. The number of NMF components and *k*-means clusters was optimized *via* MSE analysis and the elbow method, respectively. Post-processing techniques including adaptive thresholding and disc-based detection were applied to identify and classify the phases of each cluster. Multislice simulations using the Multem package were performed to support phase identification and validate experimental HAADF-STEM results.

3. Results and discussion

Epitaxial $Hf_{0.5}Zr_{0.5}O_2$ (HZO) films on perovskite substrates with $La_{0.67}Sr_{0.33}MnO_3$ (LSMO) buffer layers have been widely investigated [15,23–25]. In this study, HZO layers were deposited under conditions that yield a mixed phase microstructure to examine which crystallographic phase most strongly governs resistive switching behavior and degradation. As shown in Fig. 1a, the distinct reflections originating from STO substrate, LSMO layer (indicated by red arrows) and HZO film (indicated by dashed lines) were observed using synchrotron X-ray diffraction (XRD), indicating the oriented growth of the HZO thin film on STO substrate with LSMO buffer layer. Two distinct reflections at $2\theta = 28.4^\circ$ and 30.2°, corresponding to $(\bar{1}\ 11)$ monoclinic (m-) and (111) orthorhombic (o-) phase, respectively, suggest the textured polycrystalline nature of the epitaxial HZO thin film. The reciprocal space map (RSM) shown in Fig. 1b depicts the RSM reconstructed from a series of diffracted patterns. The regions of interest (ROIs) were selected in RSMs, which allow integration of the diffracted intensities corresponding to m- and o-phase. The reflections arising from the m-phase (white dashed rectangle) and o-phase (gray dashed rectangle) appear at $Q_z = 2.00$ Å^{-1}, 2.12 Å^{-1}, corresponding to the out-of-plane interplanar spacings of 3.14 Å and 2.96 Å, respectively. The non-zero in-plane scattering vector ($Q_x = \pm 0.075$ Å^{-1}) of $(\bar{1}\ 11)$ and (111) m-phase reflections indicates a small crystallographic tilt (interplanar angle of 87.85°) relative to the primary out-of-plane orientation, consistent with a textured, mixed variant microstructure. These observations confirm the polycrystalline nature of the HZO film.

Bright-field scanning transmission electron microscopy (BF-STEM) was employed to examine the structural morphology and interfaces of the Pt/HZO/LSMO/STO heterostructure. As shown in Fig. 1c, the thicknesses of the HZO and LSMO layers were measured to be approximately 20 nm and 34 nm, respectively. Furthermore, high-magnification high-angle annular dark-field scanning transmission electron microscopy (HAADF-STEM) images revealed the coexistence of both o- and m-phases, consistent with the XRD analysis. As shown in Fig. 1d, the atomic-scale HAADF-STEM image displayed a distinct contrast at the HZO/LSMO interface, with atomic columns clearly resolved and exhibiting well-maintained periodicity. Interplanar spacings measured from each phase were consistent with the XRD analysis, showing $d_m(111) \approx 3.12$ Å and $d_o(111) \approx 2.94$ Å, closely matching the out-of-plane interplanar spacings of 3.14 Å and 2.96 Å corresponding to the $(\bar{1}\ 11)$ m- and (111) o-phases, respectively, as previously shown in Fig. 1b. The simulated images successfully reproduced the atomic contrast and structural features observed in the experimental HAADF-STEM images, further validating the coexistence of m- and o-phases in the HZO layer (Fig. S1 and Fig. S2). Despite the polycrystalline nature of the film, individual grains (domains) exhibited well-aligned epitaxial relationships with the underlying LSMO substrate. Fast Fourier Transform (FFT) analysis of the magnified HZO/LSMO interface in Fig. S1 further revealed that the m-phase and o-phase domains correspond to [011] and [110] zone axes, respectively, with both phases aligned along the (111) out-of-plane direction of substrate. These shared crystallographic orientations and aligned FFT spots provide direct evidence that the HZO thin film is epitaxial on the LSMO substrate.

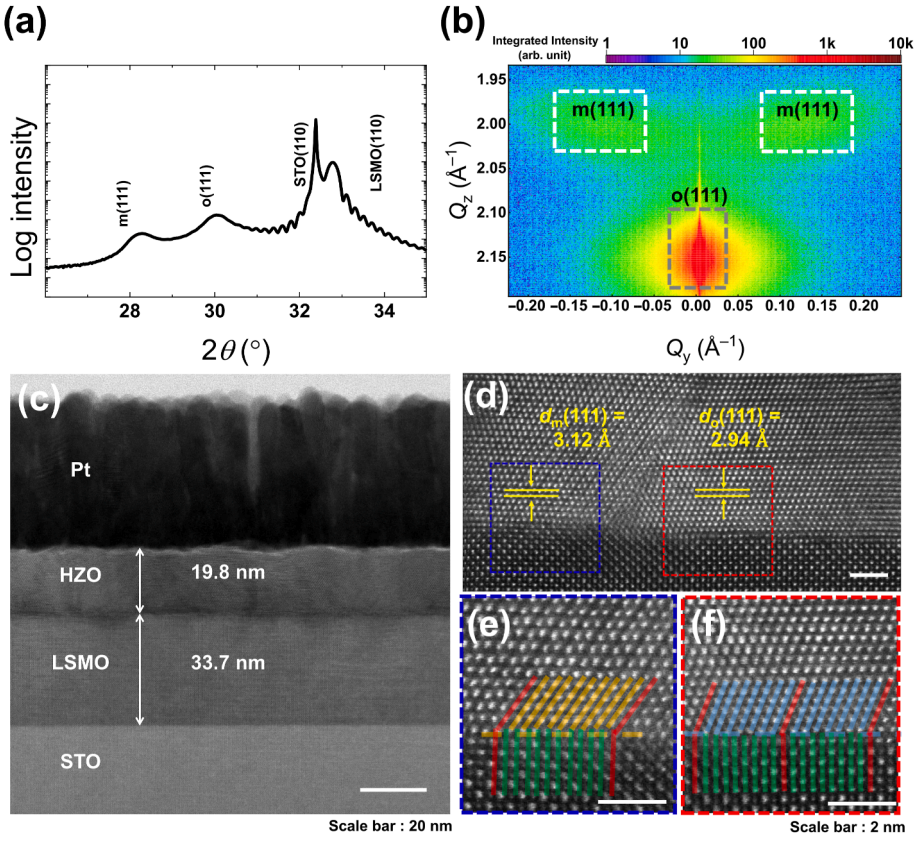

Fig. 1. Structural characterizations of HZO/LSMO thin films. (a) Synchrotron theta-2theta out-of-plane XRD scan of polycrystalline HZO sample. (b) RSM data from large number of 2-Dimensional diffracted patterns; White and gray rectangles indicate (111) monoclinic and (111) orthorhombic phase, respectively. (c) BF-STEM image of HZO/LSMO/STO sample. Scale bar, 20 nm. Detailed crystallographic of as-grown sample (d–f) HAADF-STEM image of HZO/LSMO interfaces. Scale bar, 2 nm.

However, the interface is more appropriately described as semi-coherent rather than fully coherent, because the lattice mismatch is periodically accommodated by interfacial misfit dislocations. Lattice matching ratios of 11:12 in the m-phase region and 9:10 in the o-phase region between HZO and LSMO were observed (Fig. 1d) [26]. These observations indicate that a periodic array of misfit dislocations mitigates the interfacial lattice mismatch, thereby facilitating semi-coherent growth and enabling the coexistence of m- and o-phases within the HZO thin film. Furthermore, energy dispersive X-ray spectroscopy (EDX) elemental mapping of Hf (green), Zr (purple), O (yellow), Ti (red), Sr (beige), Mn (sky blue), and La (orange) was conducted for the HZO/LSMO/STO structure (Fig. S3). The EDX results reveal sharp interfaces between each layer, with no evidence of elemental interdiffusion or contamination.

Resistive switching was evaluated over repeated DC cycles and combined pulse/DC endurance trains. As shown in Fig. S4, the HZO film containing coexisting m- and o-phase was categorized into five distinct states during the endurance test, labeled States (i), (ii), (iii), (iv), and (v). Before breakdown (States (i)-(iii)), the low resistance state (LRS) remained highly stable, while the high resistance state (HRS) exhibited notable variation across all regions. To connect electric degradation with structural evolution, *in situ* synchrotron diffraction patterns were collected at the LRS after each endurance state (Fig. 2 and Fig. S5). A pulse train was generated based on the triangular voltage waveform shown in the upper right corner of Fig. S5. Fig. 2b presents the evolution of the normalized integrated intensity ratios of the m- and o-phase diffraction signatures with electrical cycle number, obtained by integrating ROIs defined on the RSM data. Although the (111) o-phase peak intensity is often used as an approximation for orthorhombic phase content, it is also strongly affected by coherent diffracting volume, microstrain, and mosaicity. Thus, ROI integrated intensity is interpreted as a semi-quantitative metric of the coherent diffraction contribution from each phase. Throughout the endurance test, the relative integrated intensity of m-phase decreased by only 5% compared to the pristine state. In contrast, the o-phase intensity gradually declined beyond State (i), and dropped by more than 40% during the onset of breakdown (States (iv) and (v)). This suggests that repeated high-field cycling leads to degradation of the coherent o-phase crystallinity, which contributes to the rupture of the conductive filament (CF) network responsible for RS. Furthermore, since only the full width half maximum (FWHM) changed without notable shifts in the 2θ positions for both the m-phase and o-phase, it can be noted that no distinct phase transition occurred between the two phases within the experimental resolution. Instead, changes in the FWHM indicate a degradation in the crystallinity of o-phase compared to the m-phase. (Figs. S6 and S7). When sub-threshold voltages were applied, both integrated intensity ratios remained within 5% of their initial values, confirming that structural degradation is driven by high-field stimuli during the SET/RESET operations. (Figs. S8 and S9). Overall, these observations suggest that the orthorhombic phase is preferentially destabilized during cycling, and that this destabilization correlates with the progressive loss of stable resistive switching [27–29].

Fig. 3a–c presents phase mapping results obtained over a relatively wide area on the order of a hundred nanometers using 4D-STEM based nanobeam electron diffraction (NBED), designed to complement local STEM observations and to enable reliable comparison of structural degradation with XRD data. Virtual bright-field (vBF) images reconstructed from the 4D-STEM datasets are shown in Figs. S10a, S10c, and S10e, providing an overview of the sample microstructure. The phase identification was performed by using NBED patterns processed by non-negative matrix factorization (NMF) in conjunction with *K*-means clustering. The extracted data were used to generate phase cluster maps with adaptive thresholding (Figs. S10b, S10d, and S10f). The representative diffraction pattern for each cluster was integrated to extract d-spacings and interplanar angles. These values were compared with simulated patterns to determine whether the phase was orthorhombic or monoclinic. This large-area 4D-STEM/NBED analysis provides a spatial map of diffraction signatures assigned to o-like and m-like clusters. However, because automated phase assignment in multiphase polycrystalline HZO can be affected by lamella-thickness-induced overlap and classification uncertainty, we interpret these cluster maps as semi-quantitative and primarily discuss the trend in high-confidence o-like diffraction signatures with cycling [30]. Notably, cycling-induced degradation of o-phase crystallinity can reduce the sharpness/contrast of Bragg features in NBED patterns, which may cause degraded o-phase signals to be assigned to the nearest nonpolar ('m-like') cluster in

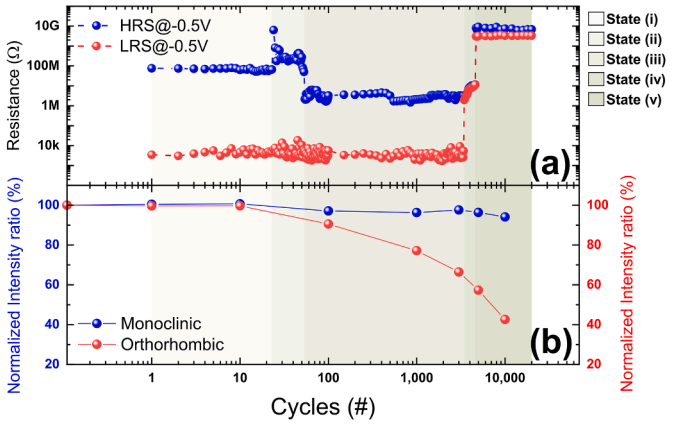

Fig. 2. Electric field-dependent (a) resistance switching behavior changes in the HRS and LRS and (b) corresponding degradation of crystallinity obtained by integrating ROIs defined on the RSM data with *in situ* XRD.

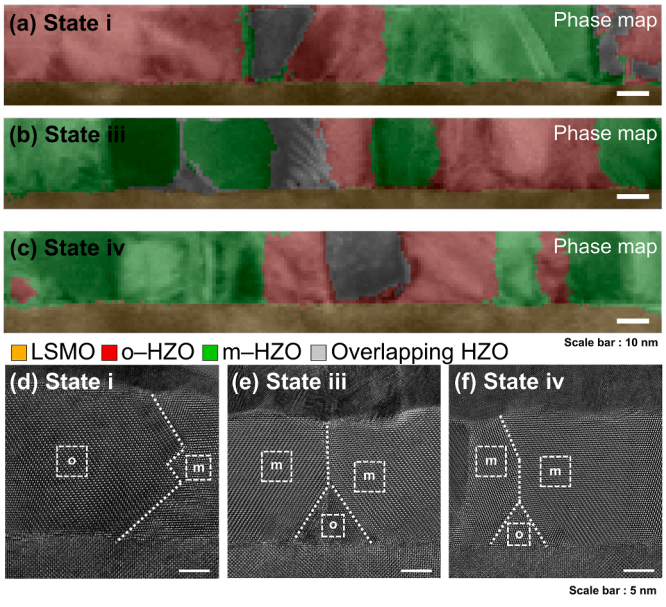

Fig. 3. (a–c) Phase mapping data acquired using NBED-based 4D-STEM, Scale bar, 10 nm. (d–f) HRTEM images for observing the localized changes of the monoclinic and orthorhombic phases at each State (i, iii, and iv). Scale bar, 5 nm.

automated workflows. This trend was consistent with the quantitative XRD, highlighting the complementarity of 4D-STEM and XRD in tracking phase evolution. While prior studies have reported cycling-induced polar-to-nonpolar phase transitions in HfO_2 based devices under certain electrode/defect conditions, our data indicate that the dominant evolution is a loss of coherent o-phase diffraction contrast, rather than a distinct phase conversion. Accordingly, the apparent reduction of o-like regions in 4D-STEM/NBED is interpreted as a decrease in unambiguous o-phase Bragg signatures, which is in line with the o-(111) peak intensity loss and broadening captured by synchrotron XRD, highlighting the complementarity of these two techniques for tracking phase evolution. Together, these techniques provide a comprehensive view of phase evolution by integrating spatial resolution with statistical robustness.

Additionally, Fig. 3d–f and Fig. S11 present HRTEM images with corresponding fast Fourier transform (FFT) analysis, which visually demonstrate localized reduction in the o-phase. Rather than implying a quantitative phase fraction change, these local analyses indicate that coherent o-phase nanodomains become smaller and more fragmented with cycling, resulting in fewer spatially continuous regions that exhibit unambiguous o-phase reflections. The accompanying FFTs in Fig. S11 index the characteristic reflections and d-spacings for each region, corroborating the phase identification and its evolution under electrical cycling. These results are consistent with the broader statistical trends identified by the 4D-STEM analysis. It is noted that the o-phase is clearly observed in State (i), however its domain size decreases in State (iii). In State (iv), the o-phase is significantly reduced, appearing only in small, confined regions between m-phase domains. Supplementary Fig. S12 shows moiré fringe images acquired from selected STEM regions in which grain contrast is clearly resolved. Grain boundaries were visually identified from discontinuities in the moiré patterns, and the projected areas of individual grains were quantified *via* pixel-based image analysis. The resulting distribution revealed the coexistence of relatively large and fine grains, suggesting that grain coarsening and phase degradation may occur concomitantly with the oxygen vacancy migration [31,32].

To investigate cycling-induced oxygen-vacancy redistribution associated with the degradation of the o-phase, scanning transmission electron microscopy coupled with electron energy loss spectroscopy (STEM-EELS) was employed to analyze the redistribution of oxygen vacancies, as the o-phase is stabilized by a high concentration of oxygen vacancies [33]. As shown in Fig. S14, the oxygen vacancy concentration within the HZO film decreases (indicated by the increase in a/b ratio in Fig. S14a) [34], while the oxygen vacancy concentration in the LSMO layer increases (indicated by the decrease in $\Delta E_{A\&B}$ in Fig. S14b) [35,36]. Since the stabilization of the o-phase requires a sufficient concentration of oxygen vacancies, this depletion may contribute to both the degradation of the o-phase structure and the rupture of CFs [34]. Furthermore, the oxygen deficiency, as revealed by the EELS analysis of the Mn valence state in LSMO, indicates that oxygen vacancies initially present in the HZO layer migrated toward the LSMO interface (Fig. S14c). This redistribution was additionally supported by STEM-EDS elemental mapping. While no significant compositional variation was observed in the LSMO layer in States (i) and (iii), spherical depletion zones became prominent in State (iv). These regions show evidence of Mn diffusion and pronounced oxygen depletion, indicating localized compositional modifications in the LSMO layer (Fig. S15). Supplementary Fig. S10f offers a comparative phase map of the HZO thin film and the underlying LSMO electrode based on cluster analysis. Initially, the LSMO maintained a single-crystalline structure, but following electrical breakdown, its crystallinity was markedly reduced. This structural deterioration, likely driven by oxygen vacancy accumulation, resulted in the fragmentation of the LSMO layer into multiple phase clusters, indicating partial polycrystallization. Damage in the LSMO region helps explain the unusual drop in current observed after breakdown in our HZO/LSMO structure. Unlike conventional memristor devices, where CFs remain continuously connected and maintain high current levels post-breakdown, the migration of oxygen vacancies and accompanying loss of electrode crystallinity suppress the conduction pathway (Fig. S4).

To investigate the current transport mechanisms, double logarithmic plot *I–V* curves were analyzed. Fig. 4a–c shows the double logarithmic plot of *I–V* plots for the States (i), (iii), and (v). In the HRS, the State (i) (initial field applications) exhibits two distinct conduction regimes as a function of applied voltage. In Fig. 4a, the State (i) follows the trap-filled-limited (TFL) conduction mechanism in the low-voltage region of the HRS. The slope of the *I–V* curve approaches 2, which typically indicates a nonlinear current increase caused by traps. Subsequently, in the LRS, the conduction follows Ohmic behavior until the RESET process occurs. Conversely, in the State (iii), the *I–V* curve for the HRS depicts three different regimes including Child's law (slope of *I–V* curve >2). Unlike TFL, which occurs when defects are dominant, Child's law arises under conditions of significantly reduced trap density (Fig. 4b). This suggests a reduction in trap sites compared to State (i). Consistent with the previous XRD and EELS results (Fig. 2b and Fig. S14), this change in the conduction mechanism is inferred to result from a decrease in oxygen vacancies caused by the degradation of o-phase [33]. Finally, in the breakdown stage, conduction becomes approximately Ohmic over the measured voltage range, consistent with substantial modification of the switching layer and electrode interface such that transport is no longer governed by reversible trap/filament modulation (Fig. 4c). When the o-phase degrades by more than 50%, the trap-site density becomes insufficient and the space-charge region contracts. Consequently, the injected carriers are dominantly thermally generated carriers. As a result, throughout the voltage sweep, only Ohmic conduction is observed to reflect the inherent characteristics of the RS layer.

Based on the combined structural and electrical results, we propose the qualitative RS mechanism of the HZO memristor, as illustrated in Fig. 4d–f. In the initial state, when a negative bias is applied for the SET process, the oxygen vacancies drift toward the Pt top electrode (TE, *i.e.*, Pt), eventually forming CFs caused by the accumulation of oxygen vacancies extending from the TE to the bottom electrode (BE, *i.e.*, LSMO). Upon applying a positive bias for the RESET process, redistribution of oxygen vacancies disrupts the pathway, leading to filament rupture. As this process is repeated, the oxygen vacancies within the HZO film progressively drift toward the BE. Once the vacancy concentration within HZO falls below a critical threshold, the formation of CFs becomes unlikely, resulting in a loss of RS behavior. Concurrent oxygen vacancy accumulation at the BE contributes to structural degradation of LSMO, further suppressing conduction and altering the breakdown electrical response.

4. Conclusions

We investigated resistive switching degradation and structural evolution in Pt/HZO/LSMO memristor by combining *in situ* synchrotron XRD under applied electric fields with *ex situ* 4D-STEM/NBED phase mapping, STEM-EELS/EDS, and electrical characterization. The orthorhombic component of the HZO layer exhibits a pronounced cycling induced loss of diffraction intensity and increased peak broadening, indicating progressive degradation of crystallinity. In contrast, the monoclinic contribution changes only

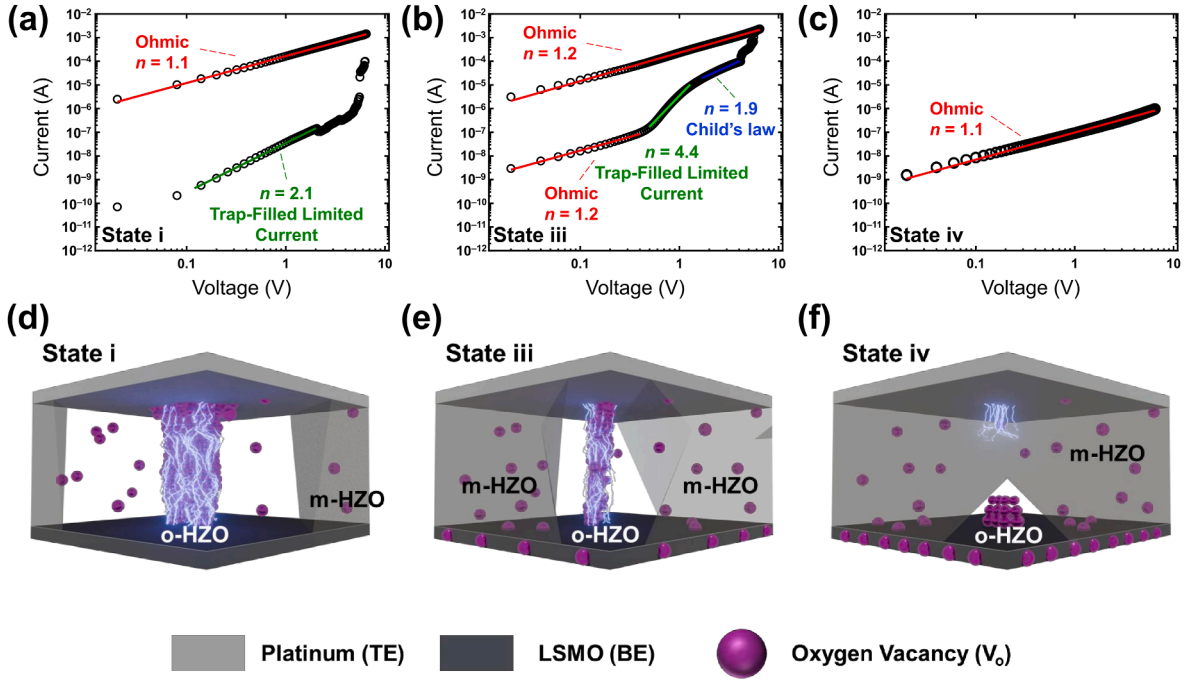

Fig. 4. Double logarithmic plots of *I–V* curves showing the current transport mechanisms at different state. (a) TFL conduction mechanism, indicated by a slope of >2 at HRS and Ohmic conduction at LRS. (b) Three distinct regions with Child's law (slope ~ 2) which suggests reduction in trap site. (c) Only Ohmic conduction, consistent with significant depletion of oxygen vacancies. (d–f) A schematic illustration of the proposed RS mechanism for the HZO memristor based on the oxygen vacancy redistribution.

modestly. Large-area NBED phase maps and local HRTEM/FFT analyses corroborate preferential reduction of orthorhombic domains with cycling. EELS/EDS results indicate that oxygen vacancies are depleted from the HZO layer and accumulate toward the LSMO bottom electrode, coinciding with degradation of electrode crystallinity after breakdown. Transport analysis reveals a transition from trap-governed conduction in early cycling to increasingly trap-poor and ultimately Ohmic behavior near breakdown, consistent with depletion of oxygen vacancy related trap sites and structural modification. These findings demonstrate that orthorhombic phase stability and oxygen vacancy redistribution jointly govern endurance and failure in HZO memristors, providing guidance for improving reliability through phase stabilization and defect engineering strategies.

CRediT authorship contribution statement

Jun-Cheol Park: Writing – review & editing, Writing – original draft, Visualization, Validation, Methodology, Investigation, Formal analysis, Data curation, Conceptualization. **WooJun Seol:** Writing – review & editing, Writing – original draft, Visualization, Validation, Methodology, Investigation, Formal analysis, Data curation. **Sihyeon Baek:** Writing – original draft, Visualization, Validation, Methodology, Investigation, Formal analysis, Data curation. **Donghyeon Lee:** Formal analysis, Data curation. **Seong Min Park:** Visualization, Formal analysis. **Seon Je Kim:** Formal analysis, Data curation. **Young-Min Kim:** Visualization, Validation, Formal analysis, Data curation. **Hu Young Jeong:** Writing – review & editing, Writing – original draft, Visualization, Validation, Supervision, Methodology, Investigation, Funding acquisition, Formal analysis, Data curation, Conceptualization. **Ji Young Jo:** Writing – review & editing, Writing – original draft, Visualization, Validation, Supervision, Methodology, Investigation, Funding acquisition, Formal analysis, Data curation, Conceptualization. **Sanghan Lee:** Writing – review & editing, Writing – original draft, Visualization, Validation, Supervision, Methodology, Investigation, Funding acquisition, Formal analysis, Data curation, Conceptualization.

Declaration of competing interest

The authors declare that they have no known competing financial interests or personal relationships that could have appeared to influence the work reported in this paper.

Acknowledgements

This work was supported by the Gwangju Institute of Science and Technology (GIST) research fund (Future-leading Specialized Research Project, 2025); by the Gwangju Institute of Science and Technology (GIST) Research Project grant funded by GIST in 2025; and by the National Research Foundation of Korea (NRF) grant funded by the Korea government (MEST) (No. 2022R1A2C201109).

Appendix A. Supplementary data

Supplementary data to this article can be found online at https://doi.org/10.1016/j.jmat.2026.101212.

References

[1] Sun K, Chen J, Yan X. The future of memristors: materials engineering and neural networks. Adv Funct Mater 2021;31:2006773.
[2] Wang Z, Li C, Lin P, Rao M, Nie Y, Song W, et al. In situ training of feed-forward and recurrent convolutional memristor networks. Nat Mach Intell 2019;1:434–42.
[3] Zhang W, Xu J, Wang Y, Zhang Y, Wang Y, Li P, et al. Nanoscaffold $Ba_{0.6}Sr_{0.4}TiO_3$: Nd_2O_3 ferroelectric memristors crossbar array for neuromorphic computing and secure encryption. J Materiomics 2025;11:101051.
[4] Mo L, Fan Z, Ou J, Chen Z, Lin H, Hu W, et al. Ultralow-power reservoir computing based on bidirectionally operable ferroelectric capacitors with tunable time constants. Rep Prog Phys 2026;89:028001.
[5] Strukov DB, Snider GS, Stewart DR, Williams RS. The missing memristor

found. Nature 2008;453:80.
[6] Corinto F, Civalleri PP, Chua LO. A theoretical approach to memristor devices. IEEE J Emerg Sel Top Circ Syst 2015;5:123–32.
[7] Chen W, Song L, Wang S, Zhang Z, Wang G, Hu G, et al. Essential characteristics of memristors for neuromorphic computing. Adv Electron Mater 2023;9:2200833.
[8] Chen S, Zhang T, Tappertzhofen S, Yang Y, Valov I. Electrochemical-memristor-based artificial neurons and synapses—fundamentals, applications, and challenges. Adv Mater 2023;35:2301924.
[9] Wali A, Das S. Two-dimensional memtransistors for non-Von Neumann computing: progress and challenges. Adv Funct Mater 2024;34:2308129.
[10] Yang N, Zhang J, Huang J-K, Liu Y, Shi J, Si Q, et al. Multitasking memristor for high performance and ultralow power artificial synaptic device application. ACS Appl Electron Mater 2022;4:3154–65.
[11] Liu Z, Cai P, Yu S, Han L, Wang R, Wu Y, et al. Investigation of time dependent dielectric breakdown (TDDB) of $Hf_{0.5}Zr_{0.5}O_2$-based ferroelectrics under both forward and reverse stress conditions. IEEE J Electron Devices Soc 2021;9:735–40.
[12] Hwang CS. Prospective of semiconductor memory devices: from memory system to materials. Adv Electron Mater 2015;1:1400056.
[13] Carta D, Guttmann P, Regoutz A, Khiat A, Serb A, Gupta I, et al. X-ray spectromicroscopy investigation of soft and hard breakdown in RRAM devices. Nanotechnology 2016;27:345705.
[14] Zhu Z, Yang H, Huang X, Wang Z, Zhang Y, Chen W, et al. Improving the synaptic behavior with polar orthorhombic phase in $Hf_{0.5}Zr_{0.5}O_2$ film. ACS Appl Electron Mater 2023;5:4682–9.
[15] Yoong HY, Wu H, Zhao J, Wang H, Guo R, Xiao J, et al. Epitaxial ferroelectric $Hf_{0.5}Zr_{0.5}O_2$ thin films and their implementations in memristors for brain-inspired computing. Adv Funct Mater 2018;28:1806037.
[16] Zeng T, Shi S, Hu K, Jia L, Li B, Sun K, et al. Approaching the ideal linearity in epitaxial crystalline-type memristor by controlling filament growth. Adv Mater 2024;36:2401021.
[17] Yang Y, Gao P, Gaba S, Chang T, Pan X, Lu W. Observation of conducting filament growth in nanoscale resistive memories. Nat Commun 2012;3:732.
[18] Vega F, Boehm A, Kim AR, Jaszewski S, Ohta T, Ihlefeld J, et al. Modifications in the charge trap landscape in $Hf_{0.5}Zr_{0.5}O_2$ as a function of oxygen vacancy concentration observed with photoemission electron microscopy. Appl Phys Lett 2025;126:152903.
[19] Wu H, Yan B, Bai G, Tang W, Zhang G, Ding Y, et al. High-temperature stability of $Hf_{0.5}Zr_{0.5}O_2$-based ferroelectric memory devices. Acta Mater 2025;294:121179.
[20] Lee D, Kim S-M, Park J-C, Jung Y, Lee S, Lee BH, et al. Enhancing reliability in oxide-based memristors using two-dimensional transition metal dichalcogenides. Appl Surf Sci 2025;679:161216.
[21] Chen H-Y, Mo C-L, Shyue J-J, Huang T-Y, Chen M-J. Probing $Hf_{0.5}Zr_{0.5}O_2$ ferroelectricity: neutron reflectivity reveals critical interface effects. ACS Appl Mater Interfaces 2025;17(10):16102–10.
[22] Park SM, Kim J, Anoop G, Seol W, Lee SY, Joh H, et al. Ferroelectric $SrMnO_3$ thin film grown on (110)-oriented PMN-PT substrate. Phys Status Solidi RRL 2024;18(8):2400025.
[23] Estandía S, Dix N, Gazquez J, Fina I, Lyu J, Chisholm MF, et al. Engineering ferroelectric $Hf_{0.5}Zr_{0.5}O_2$ thin films by epitaxial stress. ACS Appl Electron Mater 2019;1:1449–57.
[24] Jiao P, Li J, Xi Z, Zhang X, Wang J, Yang Y, et al. Ferroelectric $Hf_{0.5}Zr_{0.5}O_2$ thin films deposited epitaxially on (110)-oriented $SrTiO_3$. Appl Phys Lett 2021;119:252901.
[25] Wei Y, Nukala P, Salverda M, Matzen S, Zhao HJ, Momand J, et al. A rhombohedral ferroelectric phase in epitaxially strained $Hf_{0.5}Zr_{0.5}O_2$ thin films. Nat Mater 2018;17:1095.
[26] Estandia S, Dix N, Chisholm MF, Fina I, Sanchez F. Domain-matching epitaxy of ferroelectric $Hf_{0.5}Zr_{0.5}O_2(111)$ on $La_{2/3}Sr_{1/3}MnO_3(001)$. Cryst Growth Des 2020;20:3801.
[27] Makarov A, Sverdlov V, Selberherr S. Stochastic modeling hysteresis and resistive switching in bipolar oxide-based memory. In: International conference on simulation of semiconductor processes and devices, 237; 2010.
[28] Ilyas N, Li D, Li C, Jiang X, Jiang Y, Li W. Analog switching and artificial synaptic behavior of $Ag/SiO_x:Ag/TiO_x/p^{++}$-Si memristor device. Nanoscale Res Lett 2020;15:30.
[29] Ismail M, Ahmed E, Rana AM, Hussain F, Talib I, Nadeem MY, et al. Improved endurance and resistive switching stability in ceria thin films due to charge transfer ability of Al dopant. ACS Appl Mater Interfaces 2016;8(9):6127.
[30] Diebold AC, Ophus C, Kordijazi A, Consiglio S, Lombardo S, Triyoso D, et al. Template matching approach for automated determination of crystal phase and orientation of grains in 4D-STEM precession electron diffraction data for hafnium zirconium oxide ferroelectric thin films. Microsc Microanal 2025;31(2). ozaf019.
[31] Yamanaka J, Shirakura M, Yamamoto C, Sato K, Yamada T, Hara KO, et al. Feasibility study to evaluate lattice-space changing of a step-graded SiGe/Si (110) using STEM Moiré. J Chem Eng Mater Sci 2018;6(7):8.
[32] S'ari M, Cattle J, Hondow N, Brown R Brydson A. Low dose scanning transmission electron microscopy of organic crystals by scanning moiré fringes. Micron 2019;120:1.
[33] He R, Wu H, Liu S, Liu H, Zhong Z. Ferroelectric structural transition in hafnium oxide induced by charged oxygen vacancies. Phys Rev B 2021;104:L180102.
[34] Kang S, Jang W-S, Morozovska AN, Kwon O, Jin Y, Kim Y-H, et al. Highly enhanced ferroelectricity in HfO_2-based ferroelectric thin film by light ion bombardment. Science 2022;376:731.
[35] Kobayashi S, Tokuda Y, Mizoguchi T, Shibata N, Sato Y, Ikuhara Y, et al. Quantitative analyses of oxidation states for cubic and orthorhombic with electron energy loss spectroscopy. J Appl Phys 2010;108:124903.
[36] Rajak P, Knez D, Chaluvadi SK, Laurence R, Mechin L, Ciancio R. Evidence of Mn-Ion structural displacements correlated with oxygen vacancies in $La_{0.7}Sr_{0.3}MnO_3$ interfacial dead layers. ACS Appl Mater Interfaces 2021;13(46):55666.